

Notice

This is a non-peer reviewed preprint submitted to EarthArXiv. This manuscript has been submitted to Earth and Planetary Science Letters on Oct. 13 2019 with reference number EPSL-D-19-01403. Subsequent newer versions may differ in text and content.

Details

Title: Crack to pulse transition and magnitude statistics during earthquake cycles on a self-similar rough fault

Author: Elías Rafn Heimisson

Contact: eheimiss@caltech.edu

Crack to pulse transition and magnitude statistics during earthquake cycles on a self-similar rough fault

Elías Rafn Heimisson^{a,*}

^a*Seismological Laboratory, California Institute of Technology, Pasadena, California, USA*

Abstract

Faults in nature demonstrate fluctuations from planarity at most length scales that are relevant for earthquake dynamics. These fluctuations may influence all stages of the seismic cycle; earthquake nucleation, propagation, arrest, and inter-seismic behavior. Here I show quasi-dynamic plane-strain simulations of earthquake cycles on a self-similar 10 km long rough fault with amplitude-to-wavelength ratio $\alpha = 0.01$. The minimum roughness wavelength, λ_{min} , and nucleation length scales are well resolved and much smaller than the fault length. Stress dissipation and fault loading is implemented using a variation of the backslip approach, which allows for efficient simulations of multiple cycles without stresses becoming unrealistically large. I explore varying λ_{min} for the same stochastically generated realization of a rough fractal fault. Decreasing λ_{min} causes the minimum and maximum earthquake sizes to decrease. Thus the fault seismicity is characterized by smaller and more numerous earthquakes, on the other hand, increasing the λ_{min} results in fewer and larger events. However, in all cases, the inferred b-value is constant and the same as for a reference no-roughness simulation ($\alpha = 0$). Further, the characteristics of individual ruptures are also altered and here I highlight a new mechanism for generating pulse-like ruptures. Seismic events are initially crack-like, but at a critical length scale, they continue to propagate as pulses, locking in an approximately fixed amount of slip. I investigate this transition using simple arguments and derive a characteristic pulse length and slip distance based on roughness drag. I hypothesize that the ratio λ_{min}/α^2 could be roughly estimated from kinematic rupture models. Furthermore, I suggest that the ergodicity of planar and rough fault simulations may be different.

Keywords: Rough faults, Rate-and-state friction, Earthquake cycle simulations,
Earthquake statistics, Earthquake ruptures, Pulses
2010 MSC: 00-01, 99-00

1. Introduction

Most modeling studies of earthquakes and the seismic cycle idealize faults as planar surfaces. However, a large body of work has shown that faults and rock surfaces are not planar (e.g. Brown and Scholz, 1985; Power et al., 1987; Power and Tullis; Sagy et al., 2007; Candela et al., 2012). It has been established that fluctuations from planarity in faults are statistically fractal and self-affine (see Section 1.1 for details). It has become increasingly important to understand how and when planar models accurately capture key characteristics of individual ruptures as well as fault behavior during the entire seismic cycles.

Recently, several studies have simulated earthquakes on fractal faults. In most cases a single rupture is simulated, where the stress distribution and initial conditions are assumed before artificially nucleating the rupture (Dunham et al., 2011a; Fang and Dunham, 2013; Shi and Day, 2013; Bruhat et al., 2016). These studies have included many of the relevant physics such as off-fault plasticity and full elastodynamic effects. However, they are too computationally expensive to simulate multiple earthquake cycles which would include inter-seismic and post-seismic slip, as well as natural nucleation. This means that the assumed initial stress distribution may strongly influence the length and propagation characteristics of the simulated ruptures. A more complete approach would ideally allow stresses to evolve naturally over multiple cycles.

Other models have been developed that simulate the whole seismic cycle (Tal et al., 2018; Tal and Hager, 2018a; Ozawa et al., 2019). However, these methods lack a mechanism for stress dissipation, such as off-fault plasticity, and are purely elastic. This means that only a few cycles can be simulated before stresses build-up due to geometric incompatibility

*Corresponding author:

Email address: ehemiss@caltech.edu (Elías Rafn Heimisson)

23 and reach unrealistic values. These studies cannot investigate behavior over multiple cycles.
24 Recently, Allam et al. (2019) used the RSQsim cycle simulator to simulate seismicity on
25 a self-affine fault over multiple cycles. They used a backslip to dissipate stresses and thus
26 achieve an efficient way to simulate long term fault behavior. However, Allam et al. (2019)
27 used oversized dislocations and did not resolve the relevant length-scales that arise from
28 elasticity and the assumed friction law. Such models generally produce complex behavior
29 that becomes simpler with grid refinement (Rice, 1993; Ben-Zion and Rice, 1997). Since we
30 expect fault roughness to produce complexity, it may be hard to untangle the contribution
31 of the oversized dislocations versus the fault roughness.

32 Here I show results from a 2D plane-strain boundary element model with frictional
33 properties governed by rate-and-state friction where state evolution evolves according to the
34 aging law (Dieterich, 1979; Ruina, 1983). The simulations are quasi-dynamic and implement
35 a variation of the backslip approach to dissipate stresses. Thus unlike previous work, I
36 report results from multiple cycles without unrealistic stress build-up, but at the same time,
37 discretization is chosen such that all relevant lengths and time-scales are fully resolved. While
38 many previous studies have focused on the amplitude-to-wavelength ratio of the roughness
39 (e.g. Tal and Hager, 2018b; Bruhat et al., 2016), I focus on systematically varying the
40 minimum roughness wavelength of the fault. The range of λ_{min} explored is from 1/3 to 10
41 times the nucleation length for a planar fault.

42 *1.1. Background*

43 In this study, I investigate a strictly self-similar and statistically fractal fault. Self-
44 similarity, in this case, implies the root-mean-square (RMS) fluctuations from planarity
45 h_{RMS} are linearly proportional to the fault segment length L (Power and Tullis), in other
46 words

$$h_{RMS} = \alpha L, \tag{1}$$

47 where α is the amplitude-to-wavelength ratio. Faults that obey such self-similarity have a
 48 power spectral density (PSD) (Power and Tullis):

$$P_h(k) = (2\pi)^3 \alpha^2 |k|^{-3}, \quad (2)$$

49 where $k = 2\pi/\lambda$ is the wavenumber (λ is the wavelength). Fault roughness is often charac-
 50 terized in terms of the Hurst exponent H , where $h_{RMS} = \alpha L^H$, with $H = 1$ implying strict
 51 self-similarity. Fang and Dunham (2013) showed that for a sufficiently long wavelength slip
 52 on a self-similar fault, the average resistance to sliding due to geometric complexity is given
 53 by the roughness drag:

$$\tau_{drag} = 8\pi^3 \alpha^2 \frac{\mu}{1 - \nu} \frac{\delta}{\lambda_{min}}, \quad (3)$$

54 where δ is slip magnitude and λ_{min} is the minimum wavelength that is present in the fault
 55 profile (other symbols are defined in Table 1). The spatial extent of the slip patch must be
 56 much larger than λ_{min} for this to be valid. Roughness drag can be generalized to self-affine
 57 fault (Ozawa et al., 2019), but here I focus on the strictly self-similar case. In Section 3.1.1,
 58 I will use roughness drag to understand the certain rupture characteristic of the simulations
 59 in a quantitative manner.

60 Typically real faults are found to have α in the range of $10^{-3} - 10^{-2}$ (Power et al., 1987).
 61 The value likely depends on the maturity (cumulative amount of slip) of a fault, which the
 62 upper limit corresponding to less mature faults (Sagy et al., 2007). In this study, I have
 63 taken $\alpha = 0.01$, thus possibly representing an immature fault. This choice of α is also
 64 motivated by computational reasons since it allows interesting effects of the roughness to
 65 manifest at smaller length scales. Some studies found fault surfaces to be largely self-affine
 66 with a $H = 0.8$ in the direction of slip, but with a different slope at other scales (Candela
 67 et al., 2012). However, it has been argued that a self-similar scaling ($H = 1$) can well fit all
 68 resolvable scales simultaneously (Shi and Day, 2013).

69 The roughness drag τ_{drag} (Eq. 3) has α^2 dependence on amplitude-to-wavelength ratio,
 70 for small α the drag could be assumed small. However, the roughness drag also depends

71 on δ/λ_{min} . Implying that τ_{drag} diverges as $\lambda_{min} \rightarrow 0$ for all non-zero values of α . Clearly
72 if λ_{min} is sufficiently small, yielding of the material will occur as δ increases, thus limiting
73 the roughness drag resistance. Fang and Dunham (2013), suggested this may occur when
74 $\delta/\lambda_{min} \approx 1$. The fact that faults are found to be rough over virtually all scales suggests that
75 λ_{min} may be very small and may, therefore, be an important contributor to τ_{drag} , at least
76 up to a point when yielding occurs, that is why I have chosen to focus on λ_{min} in this study.

77 2. Model Description

78 I use a boundary element method to mesh a fault surface $h(x)$ (Figure 1). The slip on
79 each element (or dislocation) is assumed to be tangential to $h(x)$ (Figure 1d). That is, the
80 dislocation is tilted at an angle $\theta = \arctan(dh/dx)$. By use of analytical solutions for elastic
81 dislocations in full-space (Nikkhoo et al., 2016) I compute a matrix of influence coefficients
82 that relate slip vector $\boldsymbol{\delta}$ and changes in shear $\boldsymbol{\tau}$ and normal stress $\boldsymbol{\sigma}$ at the center of each
83 dislocation:

$$\boldsymbol{\tau}' = \mathbf{G}_\tau \boldsymbol{\delta}' \text{ and } \boldsymbol{\sigma}' = \mathbf{G}_\sigma \boldsymbol{\delta}', \quad (4)$$

84 where the meaning of $\boldsymbol{\delta}'$ versus $\boldsymbol{\delta}$ is discussed later. The matrices of influence coefficients
85 are compressed using the H-matrix approach of Bradley and Segall (2011). The frictional
86 interface is governed by rate-and-state friction and aging law, respectively:

$$\frac{\tau_0 + \boldsymbol{\tau}' - \eta \mathbf{V}}{\sigma_0 + \boldsymbol{\sigma}'} = f_0 + a \log\left(\frac{\mathbf{V}}{V_0}\right) + b \log\left(\frac{V_0 \boldsymbol{\theta}}{d_c}\right) \quad (5)$$

$$\dot{\boldsymbol{\theta}} = 1 - \frac{\boldsymbol{\theta} \cdot \mathbf{V}}{d_c}, \quad (6)$$

87 where \mathbf{V} and $\boldsymbol{\theta}$ represent the slip speed and state at the center of each dislocation respec-
88 tively. Eq. 5 can be rearranged to provide an approximation for the slip speed at time step
89 $n + 1$ given that the relevant fields are known at time step n .

$$\mathbf{V}_{n+1} = V_0 \exp\left(\frac{\tau_n - \eta \mathbf{V}_n}{a \sigma_n} - f_0/a - \frac{b}{a} \log(V_0 \boldsymbol{\theta}_n/d_c)\right), \quad (7)$$

Table 1: Reference parameters that are kept constant in the study

| Symbol | Description | Value |
|---|---|---|
| <i>Material properties</i> | | |
| ν | Poisson's ratio | 0.25 |
| μ | Shear modulus | 30 GPa |
| c_s | Shear wave speed | 3.5 km/s |
| <i>Friction</i> | | |
| d_c | Characteristic state evolution distance | 100 μm |
| a | Rate dependence of friction | 0.01 |
| b | State dependence of friction | 0.0125 |
| V_0 | Steady state sliding velocity | 10^{-9} m/s |
| f_0 | Steady state coefficient of friction at V_0 | 0.6 |
| σ'_0 | Initial effective normal stress | 100 MPa |
| <i>Fault</i> | | |
| α | Amplitude-to-wavelength ratio | 0.01 |
| L | Fault length along x-axis | 10 km |
| <i>Other parameters dependent on parameters above</i> | | |
| L_∞ | Critical crack half-length | $\frac{\mu d_c}{\pi(1-\nu)\sigma_0 b} \cdot \left(\frac{b}{b-a}\right)^2 \approx 29.3825$ m \dagger |
| $b - a$ | Degree of rate-weakening | 0.0025 |
| η | Radiation damping | $\mu/(2c_s) \approx 4.2857$ MPa \cdot s/m $\dagger \dagger$ |
| τ_0 | Initial shear stress | $f_0\sigma_0 + \eta V_0 \approx 60.0000$ MPa |
| θ_0 | Initial state | $d_c/V_0 \cdot (1 + \mathcal{N}(0, 0.01))$ |
| <i>Notes</i> | | |
| \dagger | (Rubin and Ampuero, 2005) | |
| $\dagger\dagger$ | (Rice, 1993) | |
| $\mathcal{N}(m, s)$ | Gaussian noise, mean m , std. s | |

90 where $\boldsymbol{\tau}_n = \tau_0 + \boldsymbol{\tau}'_n$ and $\boldsymbol{\sigma}_n = \sigma_0 + \boldsymbol{\sigma}'_n$. It is worth noting that at very high slip speeds (\sim
 91 1 cm/s) a few iteration are attempted where \mathbf{V}_n is slightly adjusted to better satisfy Eq. 7,
 92 otherwise spurious oscillations will appear. The state variable is integrated as

$$\boldsymbol{\theta}_{n+1} = \boldsymbol{\theta}_n + dt_n (1 - \boldsymbol{\theta}_n \mathbf{V}_n / d_c). \quad (8)$$

93 The time step determined by

$$dt_{n+1} = \min([\epsilon d_c / \max(\mathbf{V}_n), \epsilon \min(\boldsymbol{\theta}_n)]), \quad (9)$$

94 where ϵ is adjusted such that stability and convergence is found. The slip is updated as at
 95 each time step: $\boldsymbol{\delta}_{n+1} = \boldsymbol{\delta}_n + dt_n \mathbf{V}_n$. The problem is initialized such that $\boldsymbol{\tau} = \tau_0$, $\boldsymbol{\sigma} = \sigma_0$
 96 and $\boldsymbol{\theta} = d_c / V_0 (1 + \mathcal{N}(0, 0.01))$ at all dislocation centers (See Table 1). The fault is thus
 97 approximately at steady state $\mathbf{V} = V_0$ initially apart from small amplitude Gaussian white
 98 noise added to the initial state. A planar infinite fault with the same frictional properties
 99 will oscillate around V_0 as long as the long term average of the elastic stress transfer is
 100 $\boldsymbol{\tau}' = 0$. This is reasonable, otherwise the long term average velocity of the fault would be
 101 changing, which can only occur if the loading is changed. The problem is more complicated
 102 for a non-planar and/or finite faults if the medium doesn't dissipate the stresses (which is
 103 the case for a perfectly elastic solid) then as $\boldsymbol{\delta}$ increases so do the stresses. However, the
 104 stresses in the medium and on the fault must on average relax at the same rate as the
 105 loading rate, otherwise they would simply build up indefinitely. I approximate this process
 106 using the backslip approach (Richards-Dinger and Dieterich, 2012), where I have defined
 107 $\boldsymbol{\delta}' = \boldsymbol{\delta} - V_0 t$. Which is then used in Eq. 4 to compute the elastic stress transfer. This
 108 approach differs from the RSQsim backslip implementation (Richards-Dinger and Dieterich,
 109 2012; Allam et al., 2019), since I do not have to slip the faults backwards to determine the
 110 backslip stressing rate. I've simply formulated the problem such that the average steady
 111 state speed on the fault V_0 is also the loading rate.

112 The fault profile (Figure 1) is stochastically generated with a power spectral density in
 113 Eq. 2 using the implementation of Dunham et al. (2011a). The dislocation length projected
 114 on the x-axis was set to 1 m. The smallest $\lambda_{min} \approx 10$ m and is thus resolved in the

115 simulations. Frictional properties (see Table 1) are set such that the crack half-length which
 116 marks the transition from nucleation to a dynamic instability is constant $L_\infty \approx 30$ m and is
 117 therefore also well resolved. The fault profile was generated with λ_{min} ranging from $L_\infty/3$
 118 to $10 \cdot L_\infty$, but in all cases with the same random seed such that the Fourier decomposition
 119 at larger wavelengths is identical in both magnitude and phase.

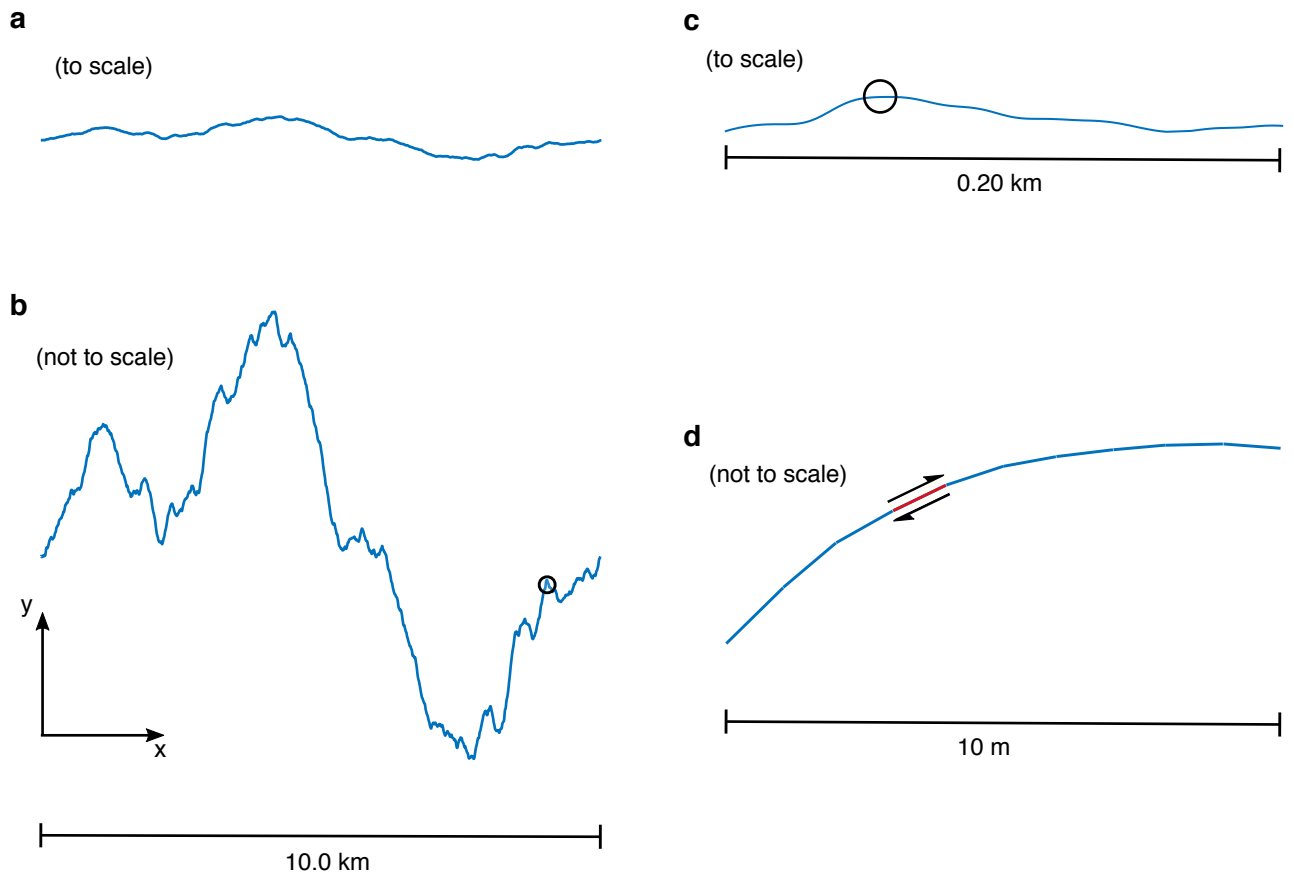


Figure 1: Fault profile at various scales for $\lambda_{min} = 2L_\infty/3$. **a** shows the entire fault at the correct length to amplitude ratio. **b** same as **a** except with exaggerated amplitude. Small circle shows the location of the fault segment shown in **c**. Circle in **c** shows the fault segment shown in **d** which displays the length scale of the discretization. Red segment shows the length of one dislocation sliding tangentially to the fault topography.

120 **3. Results**

121 *3.1. Rupture characteristics*

122 We start by visualizing the cumulative slip in all simulations (Figures 2, 3 and 4)

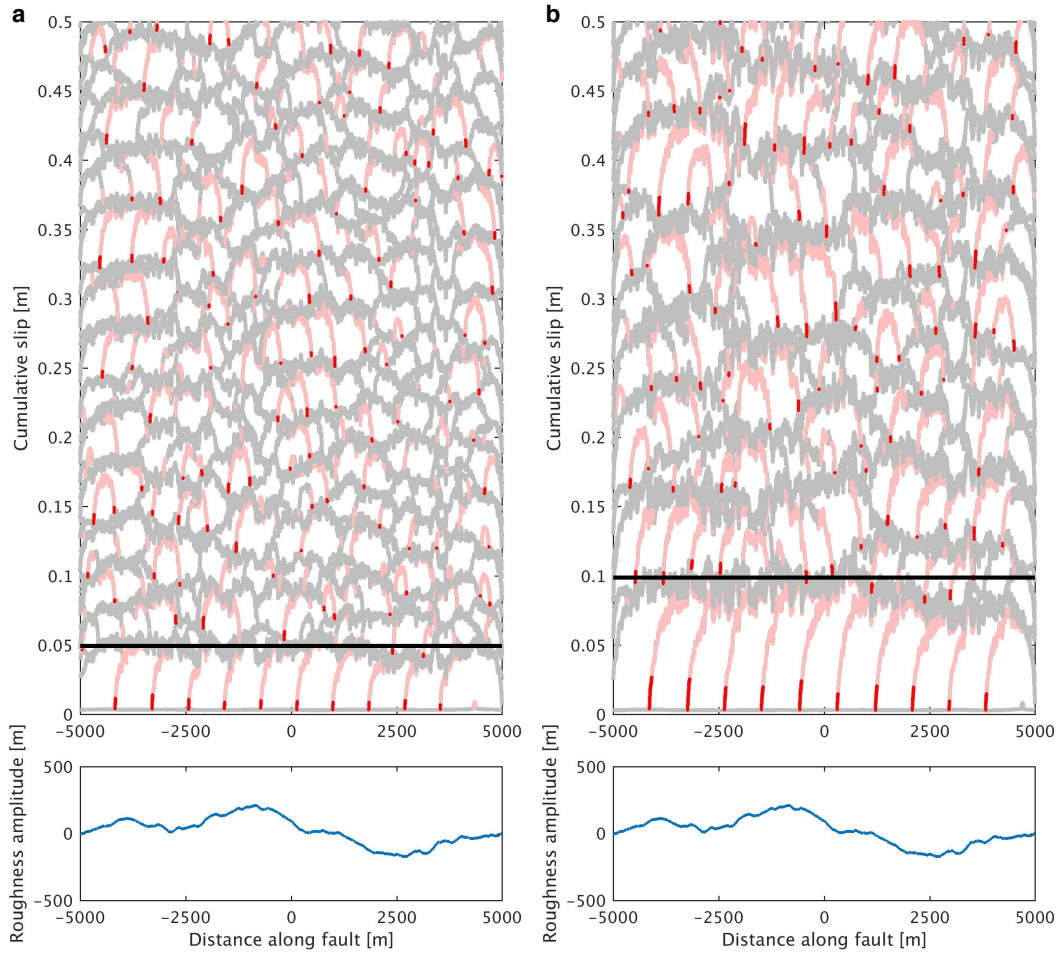


Figure 2: Snapshots of cumulative slip as a function of distance along fault. Red lines indicate points slipping faster than 1 m/s, pale pink lines indicate slip speeds larger than 1 cm/s. Grey lines are points slipping ≤ 1 cm/s. **a** shows results for $\lambda_{min} = L_\infty/3$, **b** shows results for $\lambda_{min} = 2L_\infty/3$. Bottom panels shows corresponding fault roughness, at the scale shown the fault profiles appear identical. Black line is the estimate of δ_c , the maximum slip distance estimate discussed in Section 3.1.1

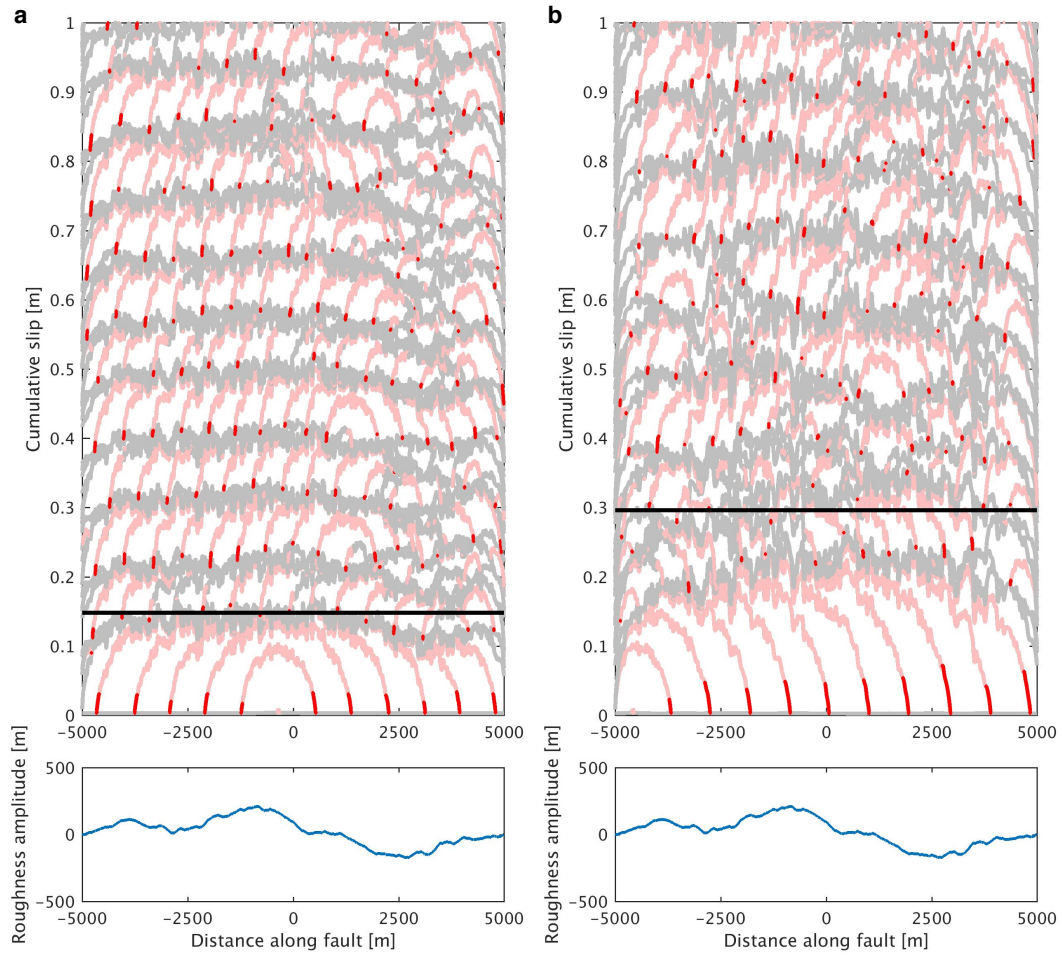


Figure 3: Same as Figure 2 except **a** shows results for $\lambda_{min} = L_{\infty}$, **b** shows results for $\lambda_{min} = 2L_{\infty}$. Note that the cumulative slip scale is different compared to Figure 2.

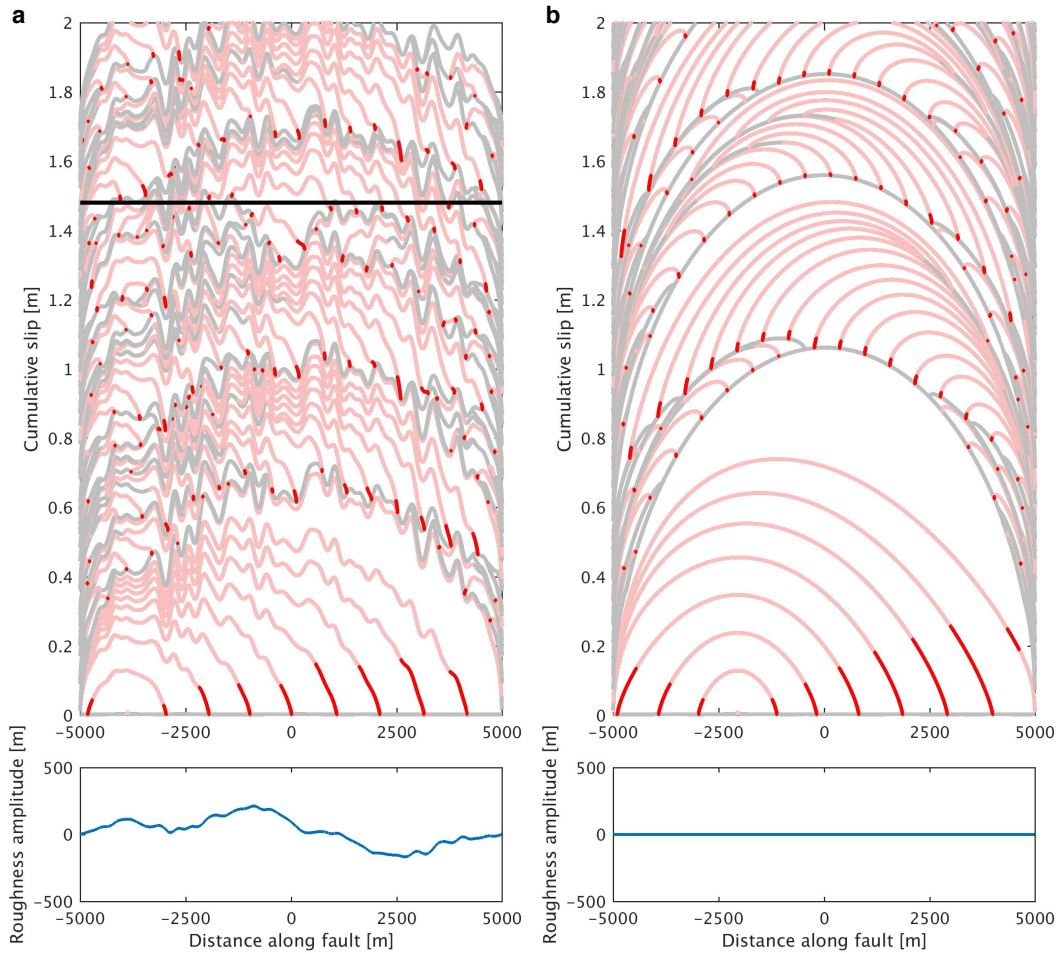


Figure 4: Same as Figure 2 except **a** shows results for $\lambda_{min} = 10L_{\infty}$, **b** shows a reference simulation of a planar fault. Note that the cumulative slip scale is different compared to Figures 2 and 3. No δ_c value exists for a planar and maximum slip distance is determined by fault finiteness and frictional properties, for **a** δ_c , significantly over-predicts the maximum slip distance because fault finiteness becomes the limiting factor before slip reaches δ_c .

123 From the slip profiles above we observe that initially the rupture always propagates
 124 the whole length of the fault. However, later events tend to be partial ruptures except
 125 when λ_{min} is large (Figure 4). Initially, the shear and normal stresses are selected to be
 126 spatially uniform, and the stress changes due to geometric complexity induced by the ac-
 127 tively propagating rupture are not sufficient to arrest the rupture. Once the initial rupture

128 has terminated, the resulting heterogeneous stress field can arrest ruptures and limits the
 129 event sizes. The results thus suggest that the assumed initial stress field in single rupture
 130 simulations on rough faults may be the primary control on the resulting rupture dimensions.

131 Another important observation from the simulations is that if events become sufficiently
 132 large, they transition from being crack-like to pulse-like, once they transition to pulse-
 133 like propagation, the events lock in an approximately fixed amount of slip. This is clear
 134 in simulations reported in Figures 2 and 3, whereas the fault in Figure 4a isn't sufficiently
 135 large to show this transition and is qualitatively similar to the planar fault simulation (Figure
 136 4b). The crack to pulse transition suggests that ruptures may have reached a length scale at
 137 which roughness drag becomes important (Eq. 3). In the next subsection, I further analyze
 138 the transition from a crack to pulse.

139 3.1.1. Crack to pulse transition

140 Let us hypothesize that transition from crack to pulse occurs approximately when the
 141 stress drop is equal to the roughness drag $\Delta\tau = \tau_{drag}$. Under these conditions it cannot be
 142 energetically favorable for a fault patch to slip further. Assuming a simple constant stress
 143 drop in-plane crack of half-length L_c then $\Delta\tau = (2\mu\bar{\delta})/(\pi(1-\nu)L_c)$, where $\bar{\delta}$ is the average
 144 slip. Setting $\Delta\tau = \tau_{drag}$ provides:

$$L_c = \frac{\lambda_{min}}{4\pi^4\alpha^2}, \quad (10)$$

145 which we interpret as a characteristic length scale for the crack to pulse transition. Re-
 146 markably, this scale only depends on roughness parameters λ_{min} and α^2 and not mechanical
 147 properties of the host rock and not the friction law, as long as the friction law favors in-
 148 stabilities that become crack-like. By comparing L_c to slip speed profiles during pulse-like
 149 propagation, we find that L_c well characterizes the dimension of the slip patch that is slipping
 150 approximately fast enough to radiating seismic energy (Figure 5). We may thus consider L_c
 151 as a characteristic dimension of the pulse. These results suggest that we may estimate L_c
 152 and therefore λ_{min}/α^2 from dynamic slip models that resolve pulse-like propagation ((e.g.
 153 Galetzka et al., 2015)). However, it is worth noting for a 3D rough surface L_c may be differ-

154 ent, at least in terms of prefactor. Further, other mechanisms can result in the manifestation
 155 of slip pulses on faults, such as low-stress conditions (Zheng and Rice, 1998), or linear sta-
 156 bility at large wavelengths due to slip to normal stress coupling (Heimisson et al., 2019),
 157 which may be responsible for generating the observed pulses in nature. It can be shown,
 158 although omitted here, that by including roughness drag in a linearized stability analysis
 159 using rate-and-state friction (e.g. Rice et al., 2001), that large wavelengths become stable
 160 (although not related to normal stress changes). This also gives a length scale $\propto \lambda_{min}/\alpha^2$,
 161 albeit with a different prefactor than L_c .

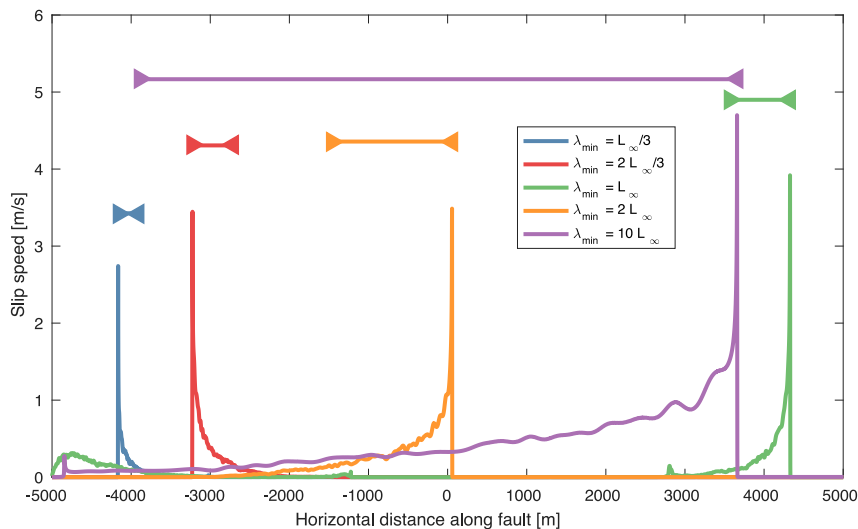


Figure 5: Comparison of L_c (horizontal lines, Eq. 10) to snapshots of slip speeds during pulse-like propagation during each simulation. The figure suggests that L_c is a good measure of a characteristic pulse length.

162 We may now use details of the rate-and-state friction law to estimate the maximum slip
 163 distance during pulse-like propagation. Once pulse reaches a point on the fault, we expect
 164 that friction rapidly evolves towards steady-state (Rubin and Ampuero, 2005). Locally
 165 the stress drop can be approximated as $\Delta\tau_{RS} \approx (b - a)\sigma_0 \log(V_d/V_0)$, where V_d could be
 166 considered a peak slip speed, here we shall take $V_d = 5$ m/s, thus $\log(V_d/V_0) \approx 22.3$. By
 167 virtue of the slow growth of the logarithm function, a minor error is introduced even if V_d
 168 is an order of magnitude smaller (in which case $\log(V_d/V_0) \approx 20.0$). Equating $\Delta\tau_{RS} = \tau_{drag}$

169 reveals a maximum slip distance δ_c before we expect roughness drag to prevent further slip

$$\delta_c = \lambda_{min} \frac{1 - \nu (b - a) \sigma_0 \log(V_d/V_0)}{\mu 8\pi^3 \alpha^2}, \quad (11)$$

170 which suggests that in a single event, $\delta \lesssim \delta_c$. The corresponding values of δ_c are plotted as
171 black horizontal lines in Figures 2, 3 and 4 for each simulation and show excellent agreement
172 with the slip magnitude in the initial event in all cases where the fault was sufficiently large
173 to manifest the crack to pulse transition properly. The crack to pulse transition reported
174 here resembles the changes in the slip distribution of simple static crack calculations done by
175 Dieterich and Smith (2009) as the crack size was increased. They also reported a maximum
176 slip distance with the same dependence on λ_{min}/α^2 as Eq. 11. However, their formulation
177 included an unknown fitting coefficient, whereas here no fitting is done.

178 *3.2. Seismicity and statistics*

179 As seen in Figures 2, 3 and 4 a single rough or planar fault can host a large distribution
180 of event sizes. In this section, I investigate the characteristics and statistics of the seismicity
181 in each simulation, in particular, the seismic moment distribution.

182 To extract discrete events from the simulations some assumptions need to be made about
183 the dimension and timing of each event. The following criteria are used for identifying a
184 single event and estimate seismic moment.

- 185 1. Identify a time period where the fault continuously slips at any point faster than 10
186 cm/s.
- 187 2. Find points where slip during that time was larger than d_c .
- 188 3. Compute the length of rupture and square to get area.
- 189 4. Compute the average change in slip where slip exceeded d_c .
- 190 5. Compute the seismic moment and magnitude

191 Clearly squaring the length of a rupture to obtain area is very simplistic and is only
192 valid if the aspect ratio of the ruptures are constant and other 3D effects, such as those that

193 might arise from event interactions, can be ignored. However, this provides a systematic
 194 way to compare our in-plane simulations to 3D observations.

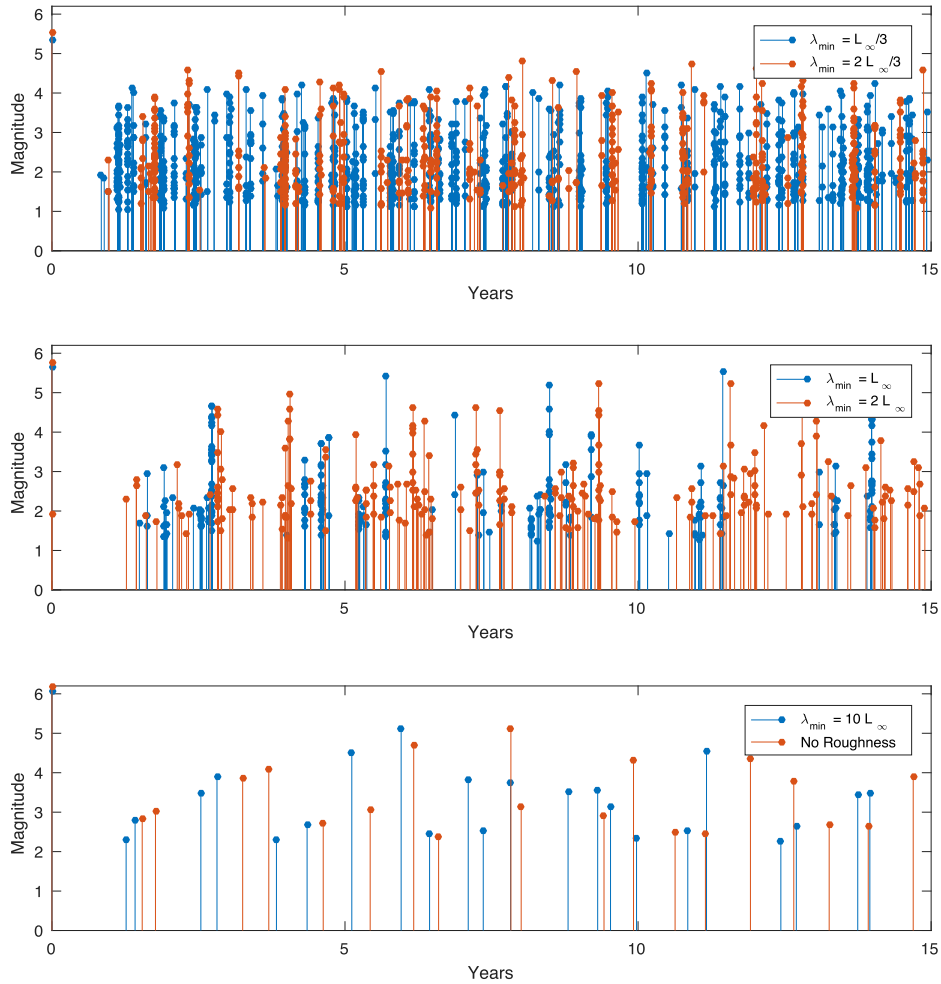


Figure 6: Magnitude versus time in all simulations for the first 15 years of simulations. For small λ_{min} , events are generally smaller and more numerous compared to larger λ_{min} values. Comparison of $\lambda_{min} = 10L_\infty$ and the no-roughness simulation reveals qualitatively similar behavior. The simulations indicated that there is both a maximum and minimum magnitude of events, which change with λ_{min} .

195 Figure 6 reveals very different frequency and magnitudes of seismicity for cases where
 196 λ_{min} is smaller or comparable to L_∞ . If $\lambda_{min} \gg L_\infty$, the results suggest that the rough fault
 197 and planar fault are qualitatively similar in terms of the frequency, timing, and magnitudes
 198 of event. Further, Figure 6 suggests that each simulation has a minimum and maximum

199 moment event. The maximum moment is easy to understand since slip cannot exceed δ_c
200 (Eq. 11), and the fault has a finite length. The minimum moment size is more mysterious
201 since by decreasing λ_{min} the minimum moment also decreased. However, by decreasing λ_{min} ,
202 the nucleation dimension should increase, which would imply that the smallest event size
203 should increase (Tal et al., 2018). A possible explanation comes from Eq. 11 where the
204 slip distance is reduced, thus limiting the sizes of the events. That explanation is not fully
205 satisfying since the smallest events in the simulations tend to arrest before reaching a slip
206 distance of δ_c . A more likely explanation may be that due to residual stresses, if λ_{min} is
207 decreased, the normal stress is locally increased at shorter wavelengths and thus locally the
208 nucleation dimension is reduced. This finding highlights the importance of the initial stress
209 in the analysis of earthquake nucleation on rough faults.

210 If the simulations presented, have any resemblance to earthquakes in nature, we expect
211 that the moment distribution of events to be a power-law. Let us compare the empirical
212 probability distribution function (PDF) to a theoretical moment distribution (Kagan, 2002):

$$\text{PDF}(M) = \frac{M_{max}^\beta M_{min}^\beta}{M_{max}^\beta - M_{min}^\beta} \beta M^{-1-\beta}, \text{ where } M_{min} \leq M \leq M_{max}, \quad (12)$$

213 where M is the moment and $\beta = 2b/3$, with b being the b value of the Gutenberg-Richter
214 distribution, where typically $b \approx 1$. For comparison with simulation we have chosen a
215 truncated moment distribution since we have inferred from Figure 6 that each simulation
216 has both a minimum and maximum moment. Comparison of the theoretical PDF (Eq.
217 12) and the empirical PDF determined from each simulation shows that the two are in
218 generally in good agreement for $b = 0.5$ (Figure 7), which well characterizes the fall-off with
219 increased moment. It generally appears λ_{min} does not control the fall-off, but as has been
220 previously noted, the truncation of the distribution is changed by λ_{min} . It is notable that
221 even for the no-roughness limit, the events follow the same power-law distribution. This is
222 consistent with recent work (Cattania, 2019), which showed in simulations and theory that
223 a planar fault that is sufficiently large could manifest a power-law distribution of events (see
224 further discussion in Section 4.1). Some interesting differences are found in Figure 7, when

225 comparing the cases of $\lambda_{min} \lesssim L_\infty$ to $\lambda_{min} = 10L_\infty$ and the no-roughness case. We notice
226 that at low values of moments the empirical distribution has gaps for $\lambda_{min} = 10L_\infty$ and the
227 no-roughness case, whereas all gaps for $\lambda_{min} \lesssim L_\infty$ occur at high moment bins when events
228 are rare. The latter is most likely due to biased sampling. The synthetic catalog includes
229 approximately the maximum event size since it is the first event that occurs (Figure 2, 3 and
230 4), but due to very numerous small events that increase computational time in these cases,
231 it was not feasible to simulate long enough sequences that would realize these rare events.
232 However, for $\lambda_{min} = 10L_\infty$ and the no-roughness case gaps occur at event sizes that should
233 have been realized in the catalog. For a larger L/L_∞ ratio these gaps might disappear. The
234 gaps in the PDF for a planar fault in Figure 7 are consistent with the bifurcation diagrams
235 by Barbot (2019), which suggest that certain values of intermediate seismic moments do not
236 occur. Based on the results in this paper I hypothesize that rough faults may be ergodic in
237 the sense that if a single simulation is run for long enough events of all possible moments
238 are realized. However, a planar fault simulation will only realize a subset of the distribution
239 of possible moments and are thus not ergodic. I conclude that more study of this topic is
240 needed, in particular in 3D.

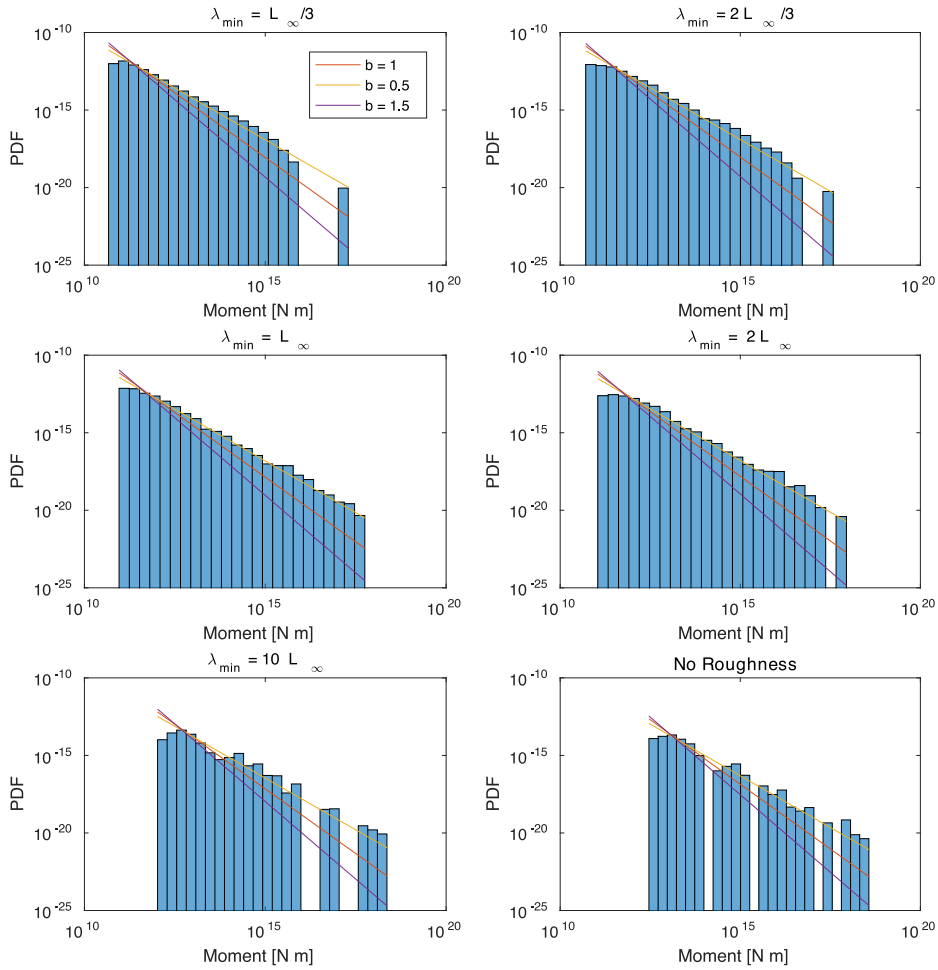


Figure 7: Comparison of Eq. 12 and the empirically estimated moment PDF function. The maximum and minimum moments in Eq. 12 are taken as the observed maximum and minimum moments in the simulations. Eq. 12 is plotted for $b = 0.5, 1, 1.5$, the comparison shows that a good agreement between empirical and theoretical PDFs is found for $b = 0.5$

241 4. Discussion

242 4.1. The b value

243 The b value most consistent with the simulations seems to be $b = 0.5$, which is consid-
 244 erably larger than the typically observed value of $b = 1$ value. The results suggest that
 245 the value is not related to the roughness since the same value is found for a planar fault,
 246 at least for $H = 1$. Cattania (2019) analyzed an anti-plane fault loaded from below by a

247 creeping velocity strengthening section and bounded from above by a free surface. Through
248 theoretical considerations of simple crack models, she argued $b = 3/4$, which was supported
249 by simulations. This value is also somewhat larger than typically observed. Cattania (2019)
250 squared the rupture lengths to attain an area, as was done here. The simplistic treatment
251 of 3D effect is thus not the source of the difference, although it may factor into what value
252 of b is determined from the simulations. The main difference in this study compared to
253 Cattania (2019) is in the fault loading, here I have simulated a finite in-plane fault that is
254 loaded using backslip, whereas Cattania (2019) loaded by deep creep and stress build-up at
255 the top was prevented by a free surface. I suggest that the difference in loading is likely the
256 cause of the difference in b value, but I conclude that this issue needs further attention since
257 it may provide insight into the physical interpretation of b .

258 *4.2. The backslip approach*

259 The backslip approach to loading and dissipating stresses is a very efficient way of sim-
260 ulating earthquake cycles for geometrically complex faults. One can argue that stresses on
261 and off faults in the earth must dissipate on average over multiple cycles at the same rate
262 as the stresses build-up due to loading. Otherwise, stress accumulation would diverge. The
263 backslip approach achieves this balance. However, the transient temporal and spatial evo-
264 lution of the stresses may not be as expected from a more rigorous model that considers
265 off-fault plasticity using a continuum model of plasticity (e.g. Dunham et al., 2011b,a; Shi
266 and Day, 2013). However, such continuum plasticity models may not be able to accurately
267 represent an important source of dissipation that occurs off the main fault on discrete struc-
268 tures such as fault branches (Ma and Elbanna, 2019). Further developments of earthquake
269 cycle simulations are needed before we can efficiently simulate multiple cycles on rough faults
270 with realistic stress dissipation mechanisms; in the meantime, backslip offers a simple way
271 to investigate these problems.

272 **5. Conclusions**

273 Roughness has an important influence on both individual ruptures and frequency and
274 magnitude characteristic of events. Events start as crack-like ruptures, but due to roughness
275 drag, they transition to pulse-like ruptures at a characteristic length-scale determined by
276 fault roughness alone and not frictional properties or material constants (Eq. 10). Pulses
277 lock in approximately spatially fixed slip distance (Eq. 11), which depends on the assumed
278 friction law and material properties. Fault roughness thus offers a plausible mechanism for
279 earthquakes to transition from cracks to pulses as they grow. I find that decreasing λ_{min} ,
280 decreases both the maximum and minimum event sizes observed in the cycle simulations,
281 however, does not appear to alter the inferred b values which remains the same even for a ref-
282 erence simulation using a planar fault. Much more numerous small events thus characterize
283 simulations with small λ_{min} compared to large λ_{min} simulation or planar fault simulations.
284 The first event in the simulations always ruptures the entire fault, but following events are
285 generally smaller partial ruptures. This difference suggests that the residual stresses induced
286 by fault roughness are paramount in determining subsequent events sizes. Caution is needed
287 when selecting the initial stress distribution for single rupture models on rough faults since
288 it may significantly influence event sizes. Finally, I've hypothesized that sufficiently rough
289 faults are ergodic, but planar faults are not, in the sense that a rough fault simulation if run
290 for long enough will manifest all possible events sizes, but a planar fault will only manifest
291 a subset of event sizes.

292 **6. Acknowledgements**

293 I want to thank Eric M. Dunham for helpful discussions on rough faults. I partially
294 conducted this research while being supported by NASA Headquarters under the NASA
295 Earth and Space Science Fellowship Program (Grant NNX16AO40H).

296 **References**

297 Allam, A., Kroll, K., Milliner, C., Richards-Dinger, K., 2019. Effects of fault roughness on coseismic slip
298 and earthquake locations. *Journal of Geophysical Research: Solid Earth* doi:10.1029/2018JB016216.

299 Barbot, S., 2019. Slow-slip, slow earthquakes, period-two cycles, full and partial ruptures, and deterministic
300 chaos in a single asperity fault. *Tectonophysics* 768, 228171. doi:[https://doi.org/10.1016/j.tecto.](https://doi.org/10.1016/j.tecto.2019.228171)
301 2019.228171.

302 Ben-Zion, Y., Rice, J.R., 1997. Dynamic simulations of slip on a smooth fault in an elastic solid. *Journal of*
303 *Geophysical Research: Solid Earth* 102, 17771–17784. doi:10.1029/97JB01341.

304 Bradley, A., Segall, P., 2011. Efficient numerical modeling of 3d, half-space, slow-slip and quasi-dynamic
305 earthquake ruptures, in: *AGU Fall Meeting Abstracts*.

306 Brown, S.R., Scholz, C.H., 1985. Broad bandwidth study of the topography of natural rock surfaces. *Journal*
307 *of Geophysical Research: Solid Earth* 90, 12575–12582. doi:10.1029/JB090iB14p12575.

308 Bruhat, L., Fang, Z., Dunham, E.M., 2016. Rupture complexity and the supershear transition on rough
309 faults. *Journal of Geophysical Research: Solid Earth* 121, 210–224. doi:10.1002/2015JB012512.

310 Candela, T., Renard, F., Klinger, Y., Mair, K., Schmittbuhl, J., Brodsky, E.E., 2012. Roughness of fault
311 surfaces over nine decades of length scales. *Journal of Geophysical Research: Solid Earth* 117. doi:10.
312 1029/2011JB009041.

313 Cattania, C., 2019. Complex earthquake sequences on simple faults. *Geophysical Research Letters* 0.
314 doi:10.1029/2019GL083628.

315 Dieterich, J.H., 1979. Modeling of rock friction: 1. experimental results and constitutive equations. *Journal*
316 *of Geophysical Research: Solid Earth* 84, 2161–2168. doi:10.1029/JB084iB05p02161.

317 Dieterich, J.H., Smith, D.E., 2009. Nonplanar faults: Mechanics of slip and off-fault damage, in: *Mechanics,*
318 *structure and evolution of fault zones*. Springer, pp. 1799–1815. doi:10.1007/s00024-009-0517-y.

319 Dunham, E.M., Belanger, D., Cong, L., Kozdon, J.E., 2011a. Earthquake ruptures with strongly rate-
320 weakening friction and off-fault plasticity, part 2: Nonplanar faults. *Bulletin of the Seismological Society*
321 *of America* 101, 2308–2322. doi:10.1785/0120100076.

322 Dunham, E.M., Belanger, D., Cong, L., Kozdon, J.E., 2011b. Earthquake Ruptures with Strongly Rate-
323 Weakening Friction and Off-Fault Plasticity, Part1: Planar Faults. *Bulletin of the Seismological Society*
324 *of America* 101, 2296–2307. URL: <https://doi.org/10.1785/0120100075>, doi:10.1785/0120100075.

325 Fang, Z., Dunham, E.M., 2013. Additional shear resistance from fault roughness and stress levels on
326 geometrically complex faults. *Journal of Geophysical Research: Solid Earth* 118, 3642–3654. doi:10.
327 1002/jgrb.50262.

328 Galetzka, J., Melgar, D., Genrich, J.F., Geng, J., Owen, S., Lindsey, E.O., Xu, X., Bock, Y., Avouac, J.P.,
329 Adhikari, L.B., Upreti, B.N., Pratt-Sitaula, B., Bhattarai, T.N., Sitaula, B.P., Moore, A., Hudnut, K.W.,
330 Szeliga, W., Normandeau, J., Fend, M., Flouzat, M., Bollinger, L., Shrestha, P., Koirala, B., Gautam,
331 U., Bhattarai, M., Gupta, R., Kandel, T., Timsina, C., Sapkota, S.N., Rajaure, S., Maharjan, N., 2015.
332 Slip pulse and resonance of the kathmandu basin during the 2015 gorkha earthquake, nepal. *Science* 349,

333 1091–1095. doi:10.1126/science.aac6383.

334 Heimisson, E.R., Dunham, E.M., Almquist, M., 2019. Poroelastic effects destabilize mildly rate-
335 strengthening friction to generate stable slow slip pulses. *Journal of the Mechanics and Physics of Solids*
336 130, 262 – 279. doi:<https://doi.org/10.1016/j.jmps.2019.06.007>.

337 Kagan, Y.Y., 2002. Seismic moment distribution revisited: I. Statistical results. *Geophysical Journal*
338 *International* 148, 520–541. doi:10.1046/j.1365-246x.2002.01594.x.

339 Ma, X., Elbanna, A., 2019. Dynamic rupture propagation on fault planes with explicit representation of
340 short branches. *Earth and Planetary Science Letters* 523, 115702. doi:[https://doi.org/10.1016/j.](https://doi.org/10.1016/j.epsl.2019.07.005)
341 [eps1.2019.07.005](https://doi.org/10.1016/j.epsl.2019.07.005).

342 Nikkhoo, M., Walter, T.R., Lundgren, P.R., Prats-Iraola, P., 2016. Compound dislocation models (cdms)
343 for volcano deformation analyses. *Geophysical Journal International* , ggw427.

344 Ozawa, S.W., Hatano, T., Kame, N., 2019. Longer migration and spontaneous decay of aseismic slip pulse
345 caused by fault roughness. *Geophysical Research Letters* 46, 636–643. doi:10.1029/2018GL081465.

346 Power, W.L., Tullis, T.E., . Euclidean and fractal models for the description of rock surface roughness.
347 *Journal of Geophysical Research: Solid Earth* 96, 415–424. doi:10.1029/90JB02107.

348 Power, W.L., Tullis, T.E., Brown, S.R., Boitnott, G.N., Scholz, C.H., 1987. Roughness of natural fault
349 surfaces. *Geophysical Research Letters* 14, 29–32. doi:10.1029/GL014i001p00029.

350 Rice, J.R., 1993. Spatio-temporal complexity of slip on a fault. *Journal of Geophysical Research: Solid*
351 *Earth* 98, 9885–9907. doi:10.1029/93JB00191.

352 Rice, J.R., Lapusta, N., Ranjith, K., 2001. Rate and state dependent friction and the stability of sliding
353 between elastically deformable solids. *J. Mech. Phys. Solids* 49, 1865–1898.

354 Richards-Dinger, K., Dieterich, J.H., 2012. Rsgsim earthquake simulator. *Seismological Research Letters*
355 83, 983–990.

356 Rubin, A.M., Ampuero, J.P., 2005. Earthquake nucleation on (aging) rate and state faults. *Journal of*
357 *Geophysical Research: Solid Earth* 110. doi:10.1029/2005JB003686.

358 Ruina, A., 1983. Slip instability and state variable friction laws. *Journal of Geophysical Research: Solid*
359 *Earth* 88, 10359–10370. doi:10.1029/JB088iB12p10359.

360 Sagy, A., Brodsky, E.E., Axen, G.J., 2007. Evolution of fault-surface roughness with slip. *Geology* 35,
361 283–286. doi:10.1130/G23235A.1.

362 Shi, Z., Day, S.M., 2013. Rupture dynamics and ground motion from 3-d rough-fault simulations. *Journal*
363 *of Geophysical Research: Solid Earth* 118, 1122–1141. doi:10.1002/jgrb.50094.

364 Tal, Y., Hager, B.H., 2018a. Dynamic mortar finite element method for modeling of shear rupture on
365 frictional rough surfaces. *Computational Mechanics* 61, 699–716.

366 Tal, Y., Hager, B.H., 2018b. The slip behavior and source parameters for spontaneous slip events on rough

367 faults subjected to slow tectonic loading. *Journal of Geophysical Research: Solid Earth* 123, 1810–1823.
368 doi:10.1002/2017JB014737.

369 Tal, Y., Hager, B.H., Ampuero, J.P., 2018. The effects of fault roughness on the earthquake nucleation
370 process. *Journal of Geophysical Research: Solid Earth* 123, 437–456. doi:10.1002/2017JB014746.

371 Zheng, G., Rice, J.R., 1998. Conditions under which velocity-weakening friction allows a self-healing versus
372 a cracklike mode of rupture. *Bulletin of the Seismological Society of America* 88, 1466–1483.